

# Analysis of Polarimetric Mini-SAR and Mini-RF Datasets for Surface Characterization and Crater Delineation on Moon

Himanshu Kumari<sup>1</sup>, Ashutosh Bhardwaj<sup>2</sup>

<sup>1</sup> Indian Institute of Remote Sensing, Dehradun, India; singh2201himanshu@gmail.com

<sup>2</sup> Indian Institute of Remote Sensing, Dehradun, India; ashutosh@iirs.gov.in

\* Correspondence: ashutosh@iirs.gov.in; Tel.: +91-9410319433

**Abstract:** The hybrid polarimetric architecture of Mini-SAR and Mini-RF onboard Indian Chandrayaan-1 and LRO missions were the first to acquire shadowed polar images of the Lunar surface. This study aims to characterize the surface properties of Lunar polar and non-polar regions containing Haworth, Nobile, Gioja, an unnamed crater, Arago, and Moltke craters and delineate the crater boundaries using a newly emerged approach. The Terrain Mapping Camera (TMC) data of Chandrayaan-1 was found useful for the detection and extraction of precise boundaries of the craters using the ArcGIS Crater tool. The Stokes child parameters estimated from radar backscatter like the degree of polarization ( $m$ ), the relative phase ( $\delta$ ), Poincare ellipticity ( $\chi$ ) along with the Circular Polarization Ratio (CPR), and decomposition techniques, were used to study the surface attributes of craters. The Eigenvectors and Eigenvalues used to measure entropy and mean alpha showed distinct types of scattering, thus its comparison with  $m$ - $\delta$ ,  $m$ - $\chi$  gave a profound conclusion to the lunar surface. The dominance of surface scattering confirmed the roughness of rugged material. The results showed the CPR associated with the presence of water ice as well as a dihedral reflection inside the polar craters.

**Keywords:** Arago, Moltke, Stokes child parameters, Decomposition techniques, Circular Polarization ratio, TMC

---

## 1. Introduction

Moon, also called Luna, is the only natural satellite of Earth. New research suggested that it came into existence nearly 4.425 billion years ago. Before humanity first set foot on the lunar surface, many uncanny theories evolved about it and its formation. Moon was assumed to be a hollow, dry barren wasteland along with another theory which called it to be an elusive fluffy rock body. All these theories and myths about Moon disappeared as the Apollo mission took place. The mission deduced that the morphological structure of the Moon filled with impact craters was formed by successive hit by meteorites and heavenly bodies. These impact craters were classified into three types i.e., simple, complex, and multiring craters. Later, Apollo's mission also deployed the evidence relating to the existence of the atmosphere present in the lunar surface. It was found that its atmosphere consists of several unusual gases including sodium and potassium along with a little number of molecules of argon, ammonia, methane, water, carbon dioxide, and equal amounts of atoms of the gases including neon, helium, and hydrogen were detected[1][2].

Several other missions were also conducted all around the world to reveal the mysteries that were revolving around our natural satellite. India’s Chandrayaan-1 and NASA’s Lunar Reconnaissance Orbiter (LRO), launched on October 22, 2008, and June 18, 2009, respectively were the first to use hybrid polarimetry. The Mini-RF and Mini-SAR sensors of these missions transmitted circularly polarized waves and received in two orthogonally polarized horizontal and vertical channels. The polarization properties of two SAR sensors contain crucial information about the physical properties of the reflecting surface[3]. The studies were done on the information provided by the missions to describe the true rocky material of the Moon. Also, it was estimated that there are possibilities of over 600 million metric tons of water ice on the Moon. The study of impact craters and water ice deposits requires the identification and extraction of craters, mare, etc. using an absolute method[4].

## 2. Material and Methods

The study area selected for this research cover parts of polar as well as non-polar regions. The craters chosen from the Northern and Southern poles include Gioja, an unnamed crater near Byrd referred to as Crater1, Haworth, and Nobile respectively. The non-polar craters include Arago and Moltke, which takes an important aspect in the study of comparing polar and non-polar regions. The datasets used are acquired by Chandrayaan-1 and Lunar Reconnaissance Orbiter (LRO) Mini-SAR besides Digital Elevation Models (DEM) products from Terrain mapping cameras (TMC). The Mini-SAR of Chandrayaan-1 worked on 12.6 cm (S-band) wavelength, 75 meters as its spatial resolution with 8km swath. Whereas LRO’s Mini-RF worked on two wavelength regions (S-band: 12.6 cm and X-band: 4.2 cm) with 30 meters per pixel resolution and 6 and 4 km swath for S- and X-bands respectively. The datasets used for this research study are given in Table 1.

Table 1: Details of the study area used for this research

S.No	Crater's name	Dataset	Satellite/Sensor	Location	Diameter (Km)
01	Gioja	fsb_01388_1cd_xiu_87n227_v1.img	Mini-SAR/Chandrayaan-1	83.3°N 2.0°E	41
02	Crater1	fsb_01261_1cd_xiu_86n354_v1.img	Mini-SAR/Chandrayaan-1	82.25°N 36.61°E	-
03	Haworth	lsz_04662_1cd_xku_86s019_v1.img	Mini-RF/LRO	86.9°S 4.0°W	51.4
04	Nobile	fsb_01657_1cd_xiu_85s066_v1.img	Mini-SAR/Chandrayaan-1	85.2°S 53.5°E	73
05	Arago	lsz_02951_1cd_xku_00s022_v1.img	Mini-RF/LRO	6.2°N 21.4°E	26.2
06	Moltke	lsz_02601_1cd_xku_01n024_v1.img	Mini-RF/LRO	0.6°S 24.2°E	6.5

The data is obtained in SAR mode, which is formatted, stored in PDS geosciences. The level -1 dataset products are level-1 Calibrated Data Records (CDRs), produced by ingesting the level-0 EDR products and associated level-0 ancillary files into the SAR processor. The level-1 CDRs are SAR images that have radiometrically and polarimetrically calibrated. Each cross-product image file

contains simple pixel lines, consisting of four 4-byte floating-point numbers. A typical Mini-SAR image strip consists of 16 bytes data in four channels of 4 bytes each given by  $|E_H|^2$ ,  $|E_V|^2$ , Real  $|E_H E_V^*|$  and Imaginary  $|E_H E_V^*|$ . The four channels represent Horizontal (H) polarization, Vertical (V) polarization, Real (Re), and Imaginary (Im) part of cross-product intensity between Horizontal and Vertical signals[5].

The Stokes vectors are measured from the architecture of hybrid polarimetry of the Mini-SAR dataset can be given as follows:

$$\begin{pmatrix} S_1 \\ S_2 \\ S_3 \\ S_4 \end{pmatrix} = \begin{pmatrix} |E_H|^2 + |E_V|^2 \\ |E_H|^2 - |E_V|^2 \\ 2 \times \text{Re}|E_H E_V^*| \\ -2 \times \text{Im}|E_H E_V^*| \end{pmatrix} \quad (1)$$

Here  $S_1$ ,  $S_2$ ,  $S_3$ , and  $S_4$  are known as Stokes parameters, where  $E_H$  and  $E_V$  represent the horizontal and vertical polarization components of the electromagnetic field respectively, and the '\*' represents the complex conjugate of horizontal or vertical polarization components. The first parameter ( $S_1$ ) describes the total intensity of the backscattered field. The second parameter ( $S_2$ ) gives the difference between horizontal and vertical components of the polarized portion of the electromagnetic field. The third and fourth parameters ( $S_3$  and  $S_4$ ) are the real and imaginary parts, representing the cosine and sine of the average phase between the horizontally and vertically polarized components of the field. They are used to describe the polarization property of the backscattered wave.

The Stokes parameters are further used to derive Stokes-child parameters like the degree of polarization ( $m$ ), the relative phase between transmitted and received signals ( $\delta$ ), and Poincare ellipticity ( $\chi$ ). These parameters are responsible to exhibit the scattering behavior of polarized waves and computed using equation 2, equation 3, and equation 4, respectively.

$$m = \sqrt{S_2^2 + S_3^2 + S_4^2} / S_1 \quad (2)$$

$$\delta = \tan^{-1} \frac{S_4}{S_3} \quad (3)$$

$$\chi = \frac{1}{2} \sin^{-1} \frac{S_4}{m \cdot S_1} \quad (4)$$

Here, in the above equations,  $S_1$ ,  $S_2$ ,  $S_3$ , and  $S_4$  are the Stokes parameters and  $m$  is the degree of polarization. These parameters are used for polarimetric decomposition as well as the Circular polarization ratio to detect the water ice regions inside the craters [6].

The Polarimetric analysis in the case of decomposition provides radar information by the scattering coherency. These techniques have also been useful for land and oceanic applications for compact Polarimetric data. The  $m$ - $\delta$  technique was proposed and developed by Raney [7]. In this technique, the degree of polarization is used to segment the total intensity into polarized and unpolarized components. The polarized part consists of surface and double-bounce scattering components and the un-polarized part is regarded as the volume scattering component. These components are given in equation 5.

$$R = \sqrt{m * S_1 * \frac{(1-\sin\delta)}{2}}$$

$$G = \sqrt{m * S_1 * (1 - m)} \quad (5)$$

$$B = \sqrt{m * S_1 * \frac{(1+\sin\delta)}{2}}$$

where R represents Double-bounce scattering, G represents Volume scattering, and B represents Surface scattering. Surface scattering seems dominant in the case of the positive value of  $\delta$ , however for the negative value of  $\delta$  double-bounce scattering is dominant. As for the volume scattering, the degree of polarization is multiplied by the total power intensity of the wave as given in equation 5.

The  $m$ - $\chi$  technique was also developed by Raney[7] with the main objective to differentiate surface from double-bounce scattering. The Electric field loses its circularity for every piece of scattering, thus considered Poincare ellipticity. Similar to the  $m$ - $\delta$  technique, the polarized part of this technique is also divided into surface and double-bounce components, and the un-polarized part is used as volume scattered component[8]. It can be expressed as an equation using a color-coded plane where R, G, and B representing Double-bounce (equation 6), Volume (equation 7), and Surface (equation 8) scattering respectively.

$$R = \sqrt{m * S_1 * \frac{(1+\sin\chi)}{2}} \quad (6)$$

$$G = \sqrt{m * S_1 * (1 - m)} \quad (7)$$

$$B = \sqrt{m * S_1 * \frac{(1-\sin\chi)}{2}} \quad (8)$$

The H- $\alpha$  decomposition technique is based on the Eigenvalue and Entropy analysis of the target coherency matrix. Entropy (H) measures the randomness of un-polarized and random components of the backscattered wave. Eigenvalues and Eigenvectors define the magnitude of scattering and the type of scattering mechanism[9]. This technique employs normalized Eigenvalues represented by probabilities for interpretation[10]. Firstly, a  $2 \times 2$  coherency matrix [J] was generated, known as the Wolf coherency matrix, given in equation 9. Each element of this matrix represents the intensity of the wave. The first matrix corresponds to the transmission of left circular polarization and reception in horizontal and vertical polarization and the second matrix is the representation of the generated coherency matrix in terms of Stokes parameters.

$$[J] = \begin{bmatrix} \langle E_H E_H^* \rangle & \langle E_H E_V^* \rangle \\ \langle E_V E_H^* \rangle & \langle E_V E_V^* \rangle \end{bmatrix} = \begin{bmatrix} S_1 + S_2 & S_3 + iS_4 \\ S_3 - iS_4 & S_1 - S_2 \end{bmatrix} \quad (9)$$

This coherency matrix [J] is used to understand the polarization properties of the backscattered wave. The eigenvalues ( $\lambda_i$ ) are generated from this matrix as given in equation 8 to embed it in the coherency matrix. Also, to obtain entropy (H), polarization states of the wave interpreted as probabilities ( $P_i$ ) are estimated using equation 10 and the value of alpha is derived from the Stokes parameters as given by equation 11.

$$P_i = \frac{\lambda_i}{\sum \lambda_i} \text{ where } \lambda_i = \sum_{i=1}^2 \frac{1}{2} (1 \pm m) \quad (10)$$

$$\alpha = \frac{1}{2} \cos^{-1} \frac{S_2}{S_1} \quad (11)$$

The matrix shown in the equation 10 shows the decomposition in terms of polarization (H) and depolarization parameter ( $\alpha$ )[9].

$$[JJ] = \begin{cases} \bar{\alpha} = \alpha(P^1 - P^2) + P_2 \frac{\pi}{2} \\ H = \sum_{i=1}^2 P_i \log_2 P_i \end{cases} \quad (12)$$

The mean alpha ( $\bar{\alpha}$ ) calculated using equation 12 is also used to characterize the scattering mechanism as done by other decomposition techniques. Different values are set to determine the scattering properties exhibited respectively where  $\alpha \rightarrow 0$  corresponds to single bounce scattering,  $\alpha \rightarrow \frac{\pi}{4}$  corresponds to volume scattering, and  $\alpha \rightarrow \frac{\pi}{2}$  corresponds to double-bounce scattering.

The stereographic Terrain Mapping Camera (TMC) ortho-imagery with a high spatial and altitude of 5 meters resolution and with 10-bit quantization has been used for this study to delineate the boundaries of the craters [11]. Table 2 describes the dataset for study area used to achieve this objective.

Table 2: TMC dataset used for crater's boundary extraction

S.No.	Orbit Number	Dataset	Resolution
01	2767	TMC_NRD_20090627T122330_1_AN.jpg	10m/pixel

The detection and delineation of crater boundaries are done using an ESRI's ArcGIS add-in crater tool and histogram-based approach. The ArcGIS crater tool is an automatic map-projection-independent tool, found precise in detecting the boundaries of craters. This tool performs two processing functions. The first process finds out the sizes of homogeneously cratered measurement areas. The second process determines the diameters of the craters through digitization. Along with this method, another approach is also used to extract the crater boundaries i.e., through histogram-based extraction. The histogram-based approach does the crater extraction based on the portioning of an image into distinct non-overlapping regions. The histogram values are selected such that the differentiation between the craters and background could be possible.

### 3. Processing and Results

The parameters and techniques described in Section-2, are essential to study and characterize the surface of the Moon through the scattering mechanism. The overall methodology is given in Figure 1.

#### 3.1. Analysis of Stokes parameters

Depending on the shape, surface roughness, orientation angle, dielectric constant, etc., the distinct type of scattering takes place. The derived Stokes parameters are used to study individual crater's surface properties as well as to compare one crater with others.

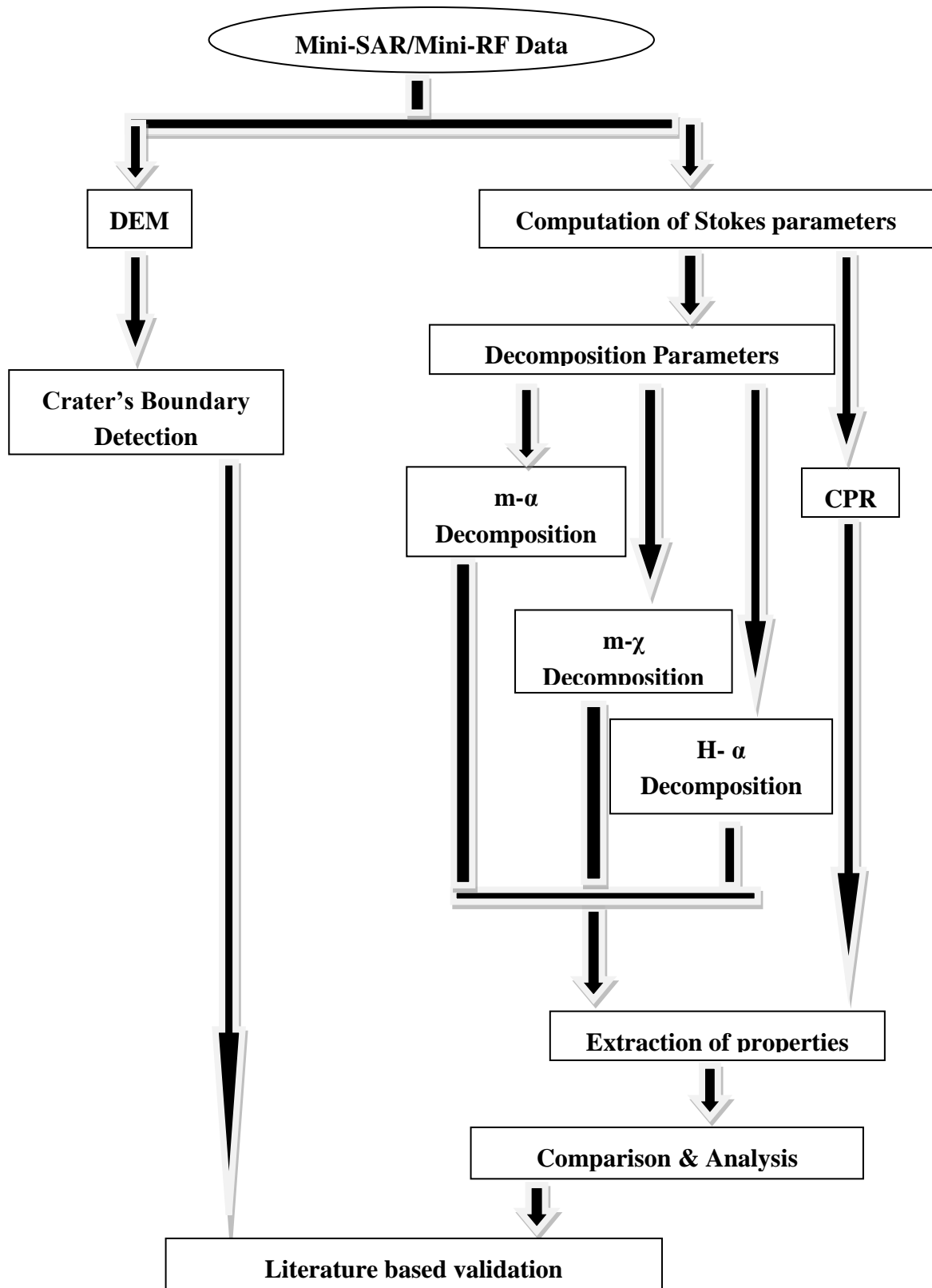


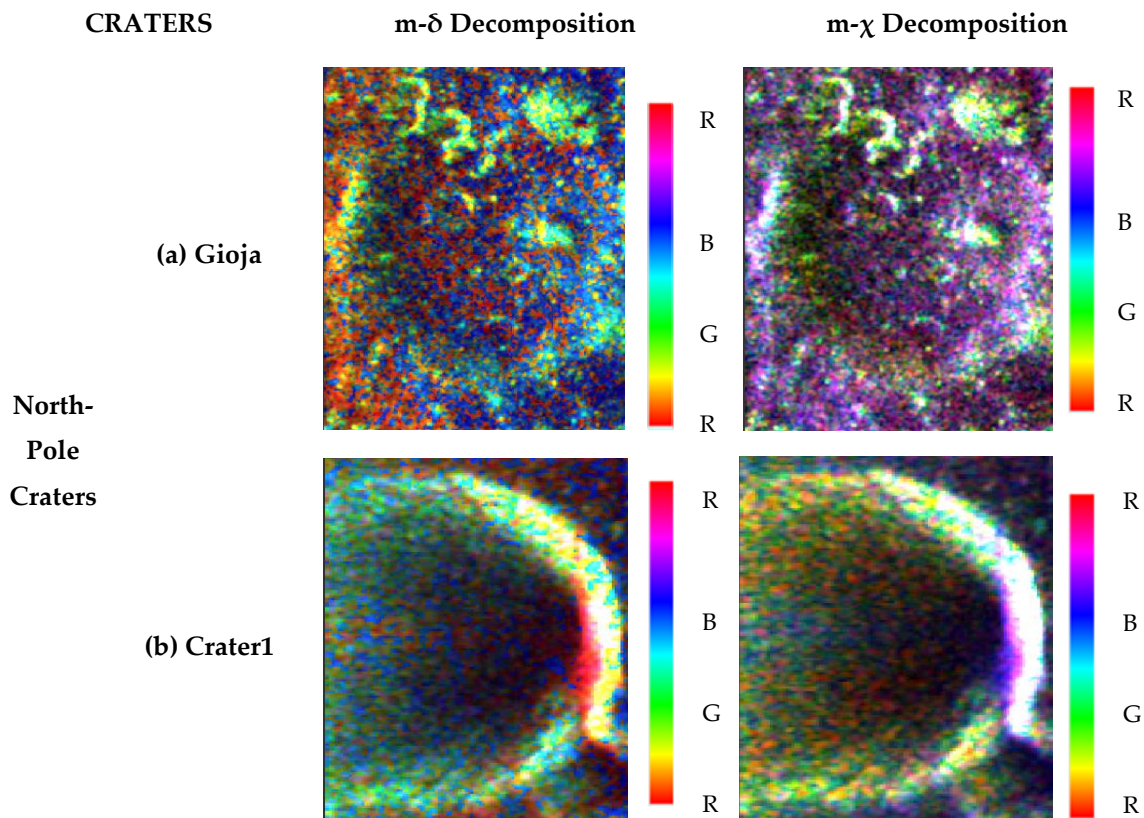
Figure 1. Overall Methodology

The degree of polarization defines the status of electromagnetic waves and the relative phase is sensitive to the variation of polarization in the backscattered signals when struck to targets. The

Poincare ellipticity states the extent of the circularity of polarization ellipse. It ranges from  $-45^\circ$  to  $+45^\circ$  which corresponds to the right and left circular polarization respectively.

### 3.2. Polarimetric Decomposition

The  $m$ ,  $\delta$ ,  $\chi$ , and  $\alpha$  parameters are used to apply the  $m$ - $\delta$ ,  $m$ - $\chi$ , and  $H$ - $\alpha$  decomposition techniques. The estimation of these parameters using Stokes parameters has been explained in Section 2. These decomposition techniques are used to retrieve scattering information of the craters' surface and sub-surface. The decomposition results characterize the surface of the craters based on the three scattering mechanisms (surface, double-bounce, and volume scattering). The scattering mechanisms have been displayed using the RGB classification plane for the individual crater in figures 2 and 3. The other colors (yellow, cyan, and magenta) also seen in the figures result from a mix of RGB palette, where the intensity of each color is the relative contribution of the components. These three scattering mechanism provides information about the surfaces of the craters which in turn helps in understanding the morphological texture of the craters. The decomposition results also provide an insight to obtain certain findings which could contribute to the presence of water ice in the deep shadowed regions of the craters.



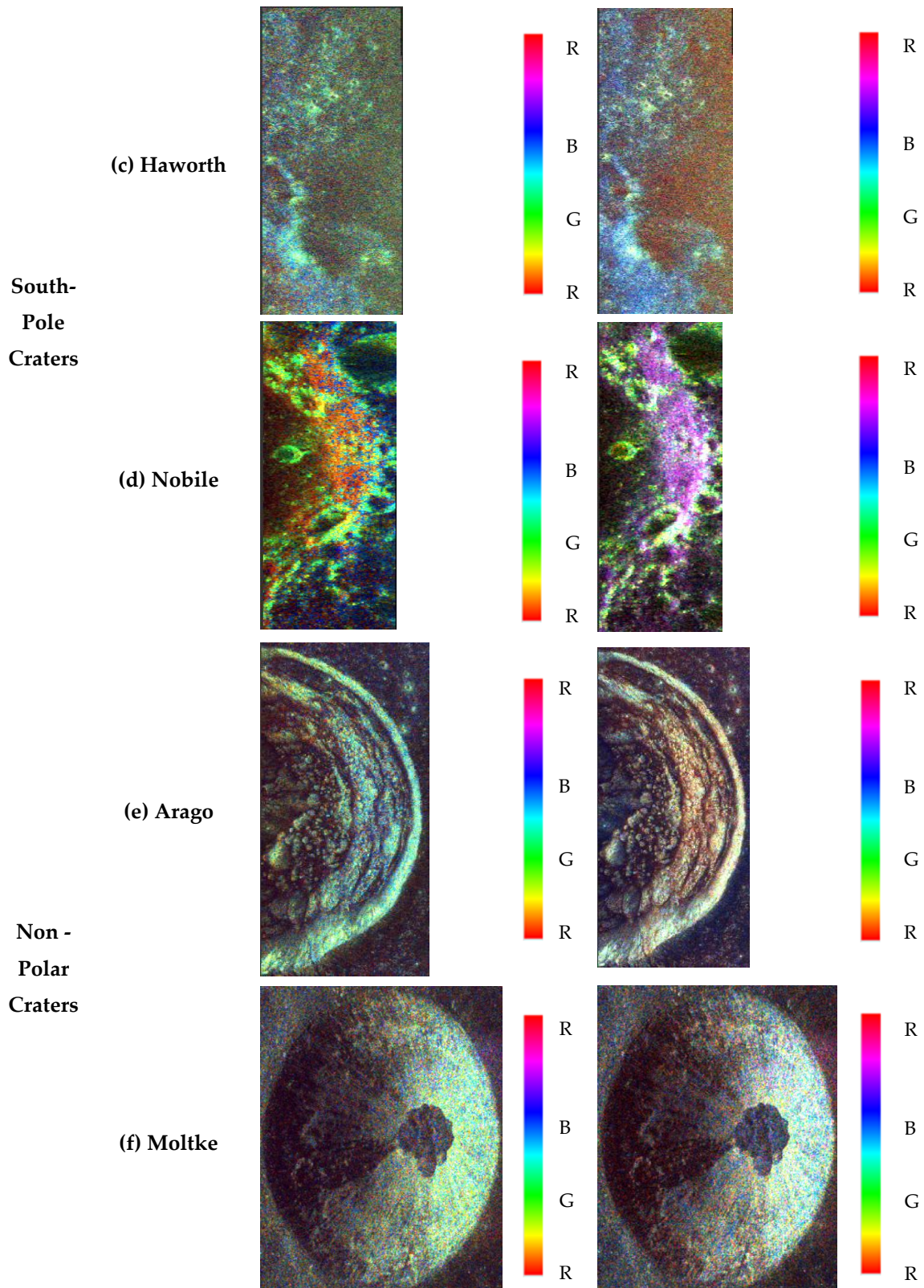
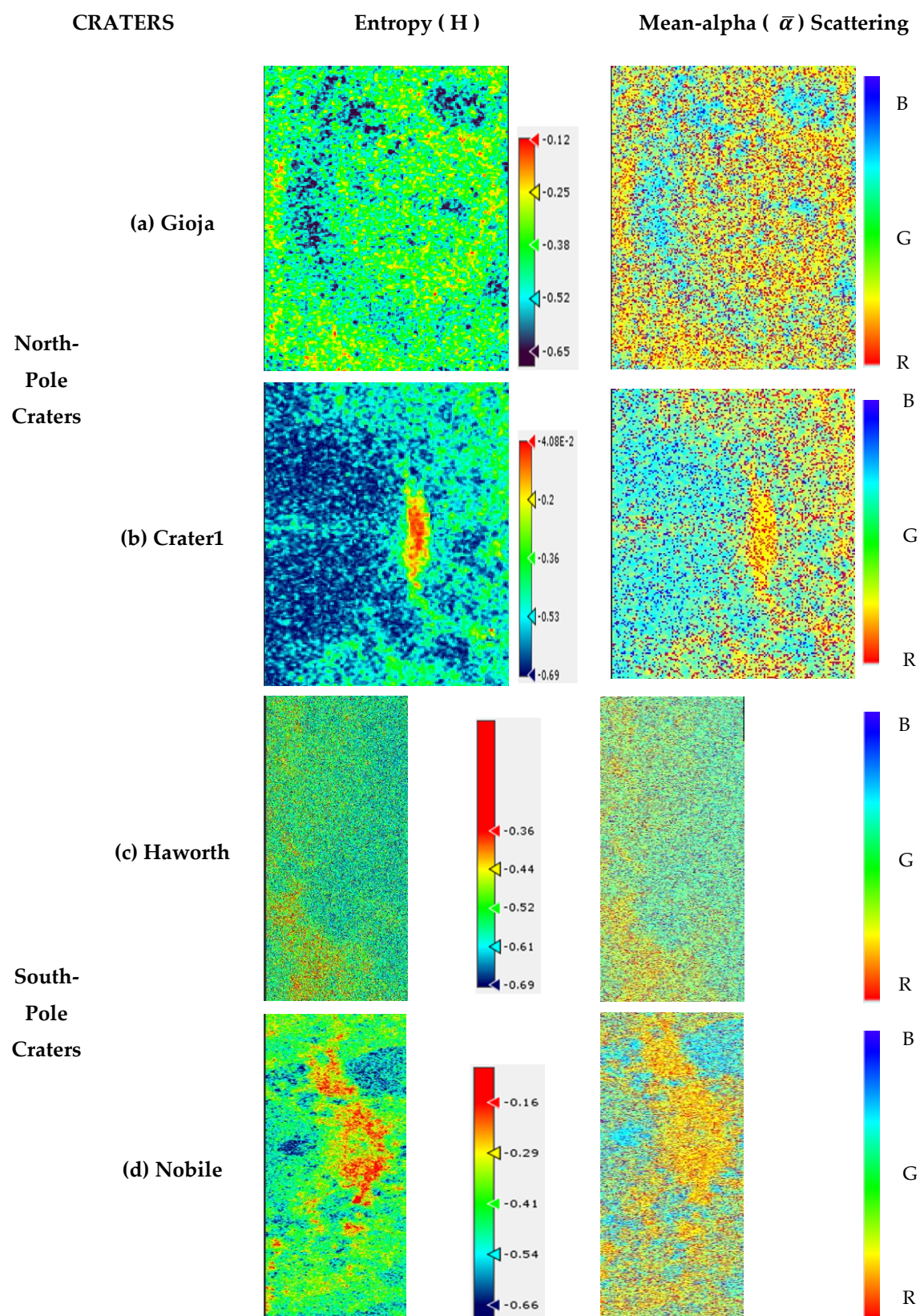


**Figure 2.** The  $m\text{-}\delta$  and  $m\text{-}\chi$  polarimetric decomposition for Gioja, Crater1, Haworth, Nobile, Arago, and Moltke craters and their surrounding region outside the craters are shown in sections (a), (b), (c), (d), (e), and (f). Here, the craters describe different scattering mechanisms where R (red color), G (green color), and B (Blue color) represents double-bounce, volumetric, and surface scattering.



The  $m-\delta$  and  $m-\chi$  decompositions shown in figure 2 describe the scattering mechanism of the crater's surface. For the Gioja crater, a high amount of double-bounce scattering is observed on one side of the outer region of the crater followed by the dominance of surface scattering observed on the other side and inner region of the crater by  $m-\delta$  decomposition. However, the  $m-\chi$  decomposition has shown a mixture of double-bounce and surface scattering in both the regions of the crater. The volume scattering is seen on the steep walls of the craters. On comparing the decomposition techniques for Crater 1, a mixture of volumetric and double-bounce scattering is seen more on the walls and inner region of the crater than the double-bounce scattering observed as few pixel regions on its walls. For the Haworth crater, both the decomposition techniques have shown almost similar results. A high amount of surface scattering is seen on the outside of this crater along with volume scattering on the irregular walls of the crater. As for the Nobile crater, several secondary craters are found inside and on its walls. The contribution of the volume scattering component is observed on the walls of the Nobile crater along with the secondary craters found on it. The region outside the crater is associated with a high amount of surface scattering, making this surface smoother as compared to other regions. The  $m-\delta$  decomposition has shown the high intensity of double-bounce inside the crater while a mixture of double-bounce and surface scattering is observed in the same region by  $m-\chi$  decomposition. On comparing the texture of the inner and outer region of the crater, since more double-bounce and volume scattering is observed, therefore it can be said that the inner region is rougher as compared to the outer region, which could be due to the reflection of backscattered wave after striking the regions of the secondary craters. As for the non-polar craters, high intensity of volumetric and double-bounce scattering is observed on the ring-like walls of the Arago crater by  $m-\delta$  and  $m-\chi$  decompositions respectively. Similar results are also found for the Moltke crater, associating with the combination of double-bounce and volume scattering on its walls. The scattering mechanism has shown the dominance of surface scattering outside both crater regions. Since the non-polar craters are present on the Lunar Mare region, the outer region of these craters can be expected to have a smoother surface.

For most of the craters, both these decomposition techniques have shown different results in terms of the contribution of scattering components. So, the roughness and smoothness of the surface of craters cannot be verified with these results alone, thus the additional technique is used to understand the scattering mechanism properly. The  $H-\alpha$  decomposition is applied to the same craters to see its contribution to the backscattered signal and find out the intensity of scattering components.



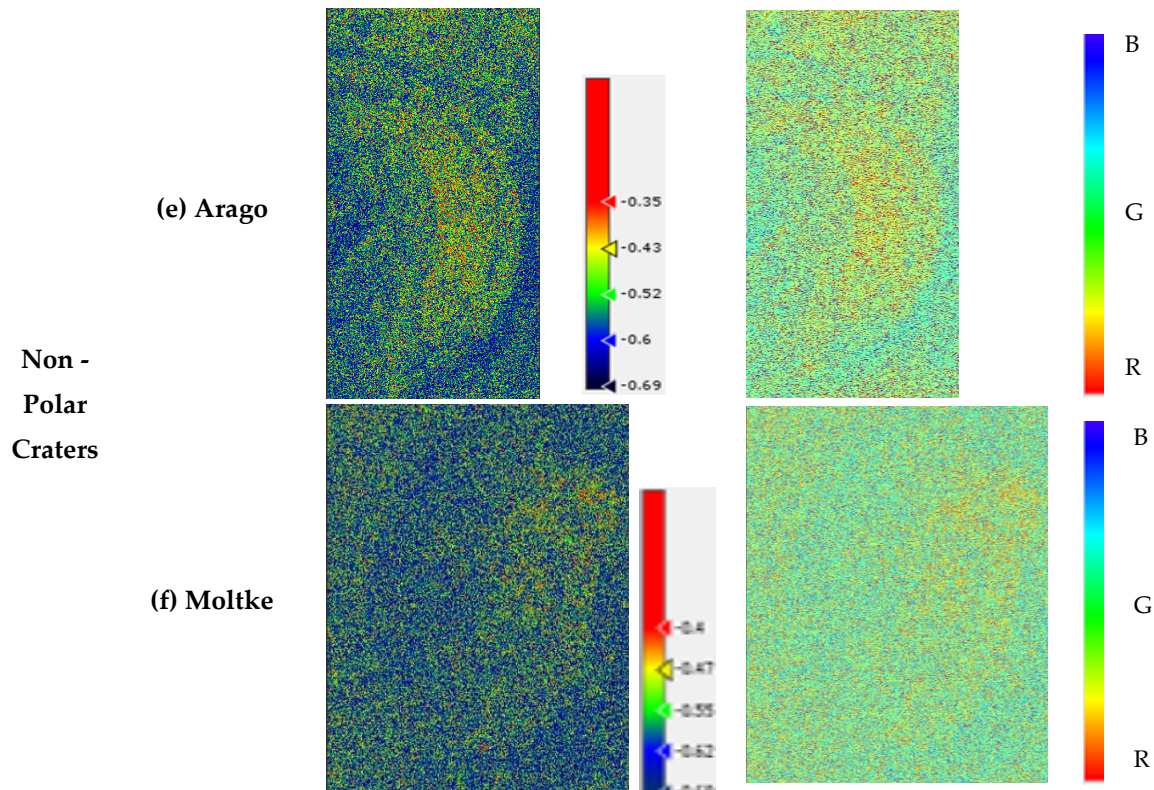


**Figure 3.** The entropy (H) and mean-alpha angle ( $\bar{\alpha}$ ) for all the craters including Gioja, Crater1, Haworth, Nobile, Arago, and Moltke craters are shown by (a), (b), (c), (d), (e), and (f) where B, G, R represent the surface, volume, and double-bounce scattering respectively.

The H- $\alpha$  decomposition technique comprises entropy (H) and auxiliary angle ( $\alpha$ ) parameters which help in analyzing the behavior of the surfaces of craters. The entropy component is responsible for describing the degree of polarization and the mean-alpha component is used to understand the type of scattering associated with the surface. Both these parameters are combined and interpreted in terms of the scattering mechanism to understand the surfaces. For the Gioja crater, the high degree of entropy is found at few regions present inside and outside the crater, associating them with double-bounce and mixture of volume and double-bounce scattering. The walls of this crater have contributed to the low value of entropy and associated with surface scattering. As for Crater 1, a low value of entropy with a high amount of surface scattering is observed within the crater. However, a mixture of double-bounce and volume scattering with moderate entropy is observed outside the crater region which relates to high roughness in terms of texture properties. In the entropy imagery of figure 3 (b), the high intensity of double-bounce scattering associating with high entropy value is observed on its walls. On comparing the entropy and mean-alpha parameter of Haworth crater, the dominance of volume scattering followed by surface scattering is seen within the crater whereas a little amount of double-bounce scattering is found outside the crater region. In figure 3 (d), more contribution of double-bounce and mixture of volume and double-bounce scattering is observed on the walls of the Nobile crater, associating with high entropy values that correspond to greater roughness. Surface scattering is observed at low entropy values inside the region of the Nobile crater. As for the non-polar crater named Arago and Moltke, low values of entropy with high

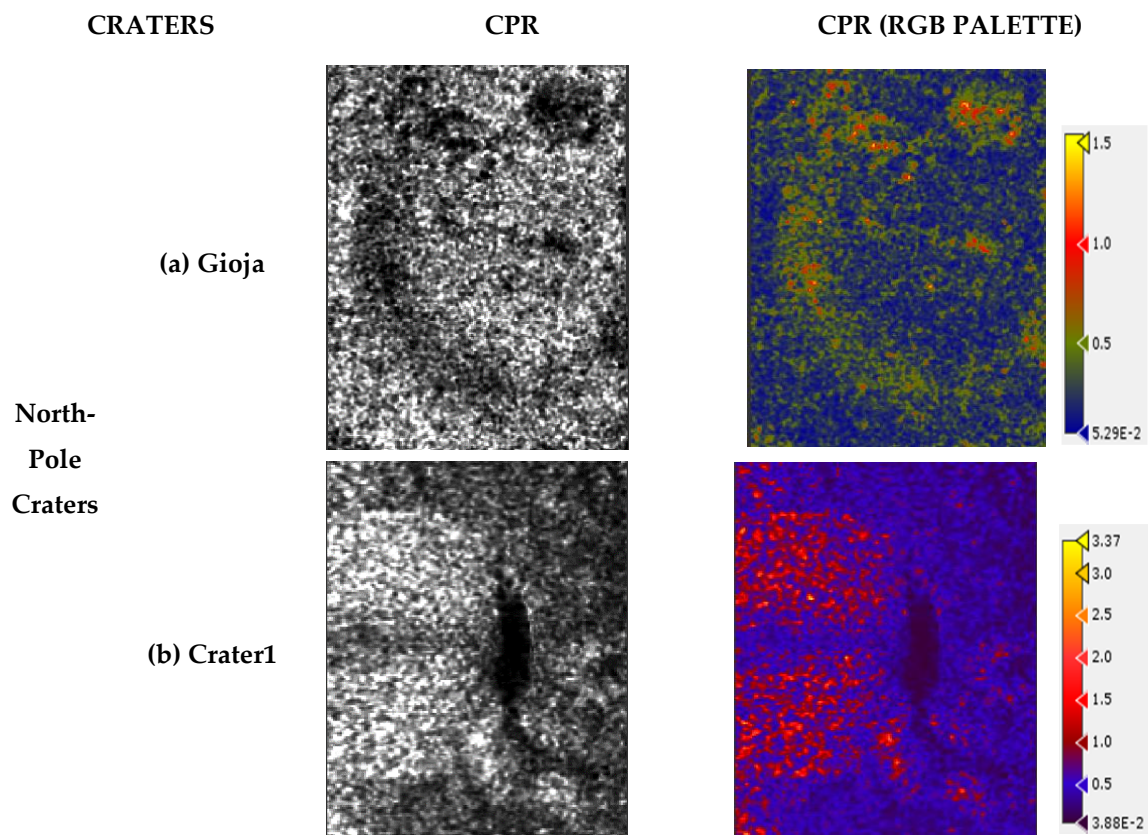
volume scattering are found within and outside the regions of the craters. High entropy values associating with double-bounce scattering are observed on the ring-like walls of the craters. The high amount of volume scattering found in most crater regions corresponds to the high backscatter intensity which could relate to either the presence of water ice deposits or more roughness due to reflection by natural dihedrals. To find the presence of water ice in the surface or sub-surface of the craters, the Circular Polarization Ratio (CPR) is calculated and then it is compared with the scattering mechanism for analysis.

### 3.3. Analysis of water ice deposits

CPR is defined as the ratio of the received power in the same sense polarization (SC) with received echo in the opposite sense of circular polarization (OC). It is also known to be a robust indicator of surface roughness. It can be determined using equation 8.

$$CPR = \frac{(S_1 - S_4)}{(S_1 + S_4)} \quad (10)$$

A low value of CPR (less than 0.4) indicates a smooth texture of the surface and a rough surface is indicated as double-bounce with higher CPR value. However, a CPR value greater than 1 strongly indicates the possibility of presence of water ice deposits present on the surface.



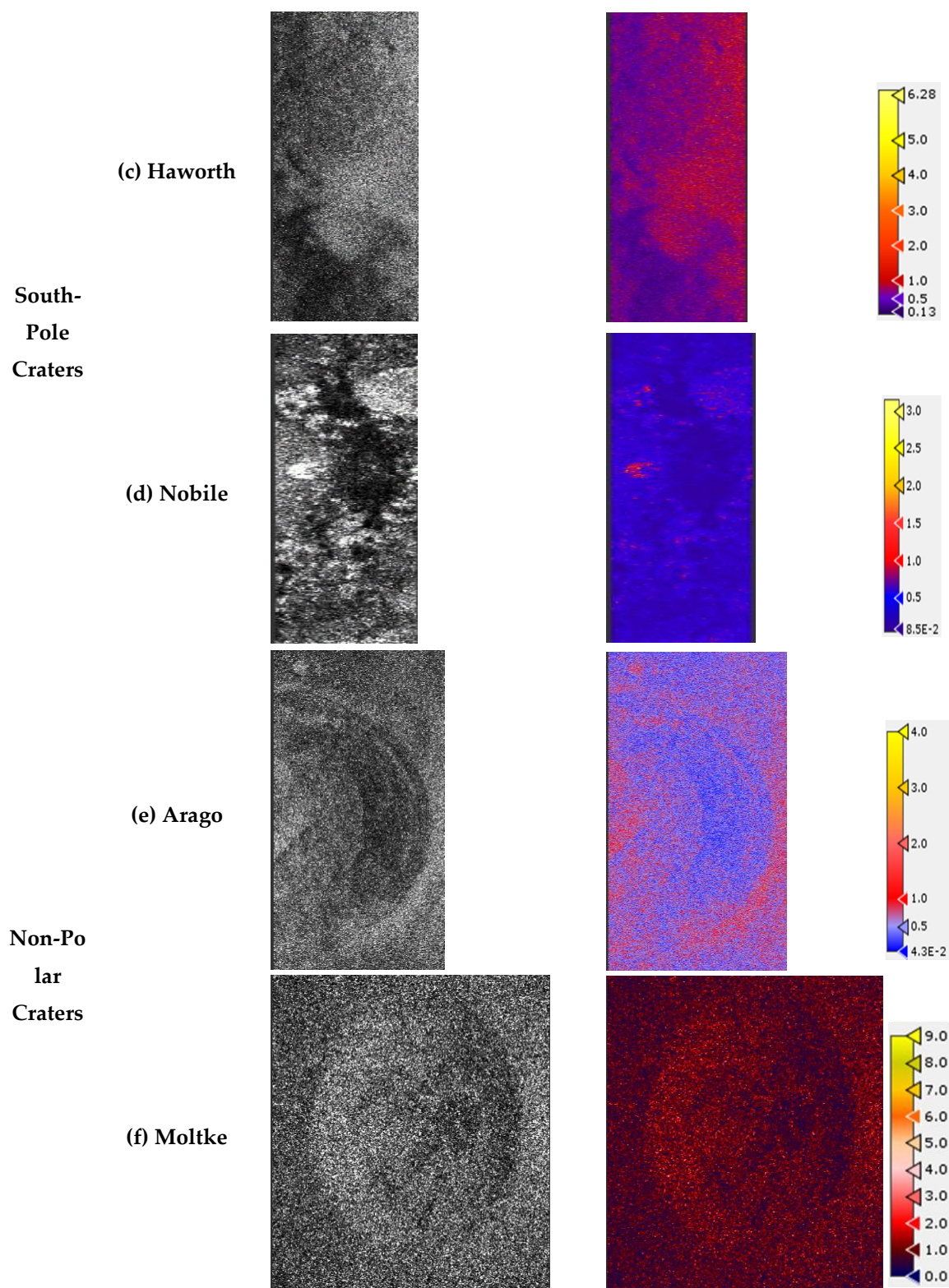


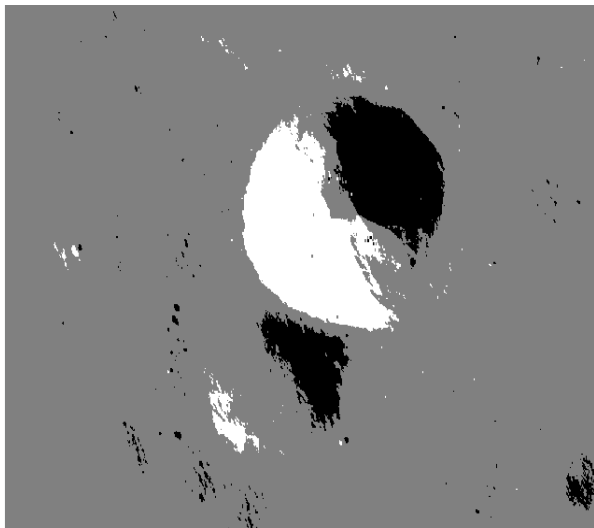
**Figure 4.** The CPR results along with their values for the polar craters are shown for (a) Gioja, (b) Crater1, (c) Haworth, (d) Nobile, and non-polar craters including (e) Arago and (f) Moltke respectively.

The CPR results for polar and non-polar craters namely Gioja, Crater 1, Haworth, Nobile, Arago, and Moltke are shown in figure 4. The regions of the polar craters have shown their CPR values reaching up to +1.5 and +3.37 for Gioja and Crater1, and +6.28 and 3.0 for Haworth and Nobile

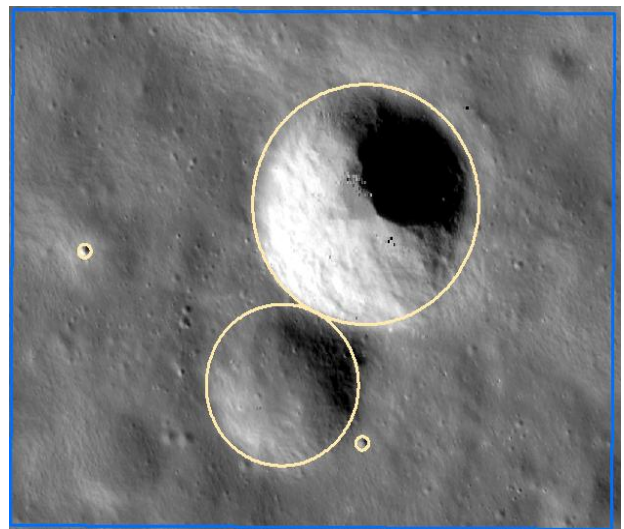
respectively. However, the peak value of the CPR is obtained for the non-polar craters consisting of Arago and Moltke with +4.0 and +9.0 respectively. The results have shown very high CPR values for all the craters which could either be due to the presence of water ice deposits or reflection from natural dihedrals. Since CPR values result from variation in the backscatter intensity of the respective surfaces, the scattering mechanism could play a crucial role in determining the true regions of water ice deposits by relating it with CPR values. After proper analysis, it is found that the walls of the Gioja crater and inner region of Crater1 contribute to the volume scattering mechanism with high CPR values. As for the Haworth and Nobile crater, the high CPR along with the contribution of volume scattering is observed within the crater regions. Therefore, these respective regions of the craters could be concluded for the presence of water ice deposits. For the Arago and Moltke crater, the contribution of pure volume scattering component is not observed anywhere in the crater regions instead double-bounce scattering is seen which concludes to high surface roughness. Thus, it is concluded that the high CPR values in the regions of these craters are due to reflection by natural dihedrals.

#### 3.4 Crater Boundary Extraction

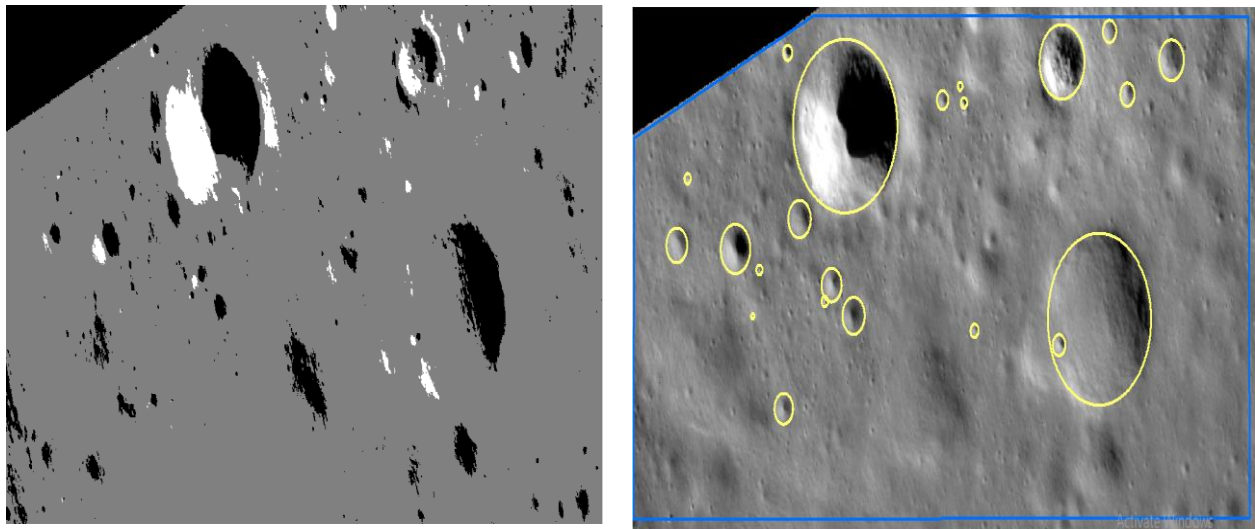
The study area used for boundary delineation is subsetting in two regions, from which the impact craters are drawn using crater boundary extraction techniques. The boundary extraction of the craters is done using two approaches ArcGIS Crater tool and histogram-based extraction. The results obtained by using these methods are shown in figure 5.



(a)



(b)






(c)

(d)

**Figure 5.** Detected crater boundaries using (a), (c) Histogram-based extraction, and (b), (d) ArcGIS Crater Tool for two regions subsetted from the study area.

**Table 3.** Threshold values assigned for Histogram-based extraction technique

Colors	Values Assigned (a)	Values Assigned (b)
	0-75	0-75
	75-177	75-147
	177-358	147-279

The histogram-based detection is based on the threshold given to a particular set of regions to differentiate between the craters and the background. The intensity values of the craters and the background are recorded and the most intermediate values at the inner and the outer regions of the crater were decided. These intermediate values are used to divide the histogram into two classes as given in table 3.

The extracted circular boundaries using the ArcGIS Crater tool are shown by the circles in figure 5-(b), and 5-(d). The best fit circular boundaries of the craters are drawn by marking three points around their circular rim. Along with the manual marking of the craters via 3-point features, a grid of 500 meters is formed around those craters. The measurement grid helped with the investigation of large measurement areas using the crater digitization approach cell by cell [12]. The coordinates of the craters extracted using the ArcGIS Crater tool is given in table 4 and 5.

Table 4. Details including diameter and central coordinates of extracted craters of study area (a)

S.NO.	DIAMETER (KM)	X COORDINATE	Y COORDIANTE
01	1.937058	113.4339	85.13826
02	1.303399	113.3224	85.14931
03	0.109765	113.4989	85.15936
04	0.111583	113.248	85.14534

Table 5. Details including diameter and central coordinates of the extracted craters of study area (b)

S.NO.	DIAMETER (KM)	X COORDINATE	Y COORDINATE
01	1.045988	114.7418	85.13961
02	0.090876	114.8095	85.14265
03	0.297324	114.7193	85.15133
04	0.449713	114.6829	85.12048
05	0.202425	114.6558	85.14431
06	0.223233	114.6283	85.14320
07	0.226255	114.7082	85.14543
08	0.033638	114.6726	85.15145
09	1.035537	114.5182	85.12321
10	0.246501	114.6357	85.11152
11	0.140828	114.6353	85.11588
12	0.134382	114.6795	85.11592
13	0.062078	114.7025	85.12940
14	0.113712	114.7136	85.13109
15	0.050187	114.7138	85.12935
16	0.127701	114.5209	85.12709
17	0.063523	114.7814	85.15366
18	0.209399	114.7475	85.15603
19	0.059789	114.6965	85.14986
20	0.066793	114.6493	85.14522
21	0.080837	114.5662	85.13367



After proper analysis, it is concluded that the histogram-based approach for the crater's boundary extraction was not able to delineate the precise boundaries of the craters. This is due to the eroded irregular structures and ejecta flow of the craters that it is found difficult to provide differentiated values for craters and the background. However, in the case of delineation through the ArcGIS tool, the craters are extracted along in a much better way but this technique only seemed to work for circular craters.

#### **4. Discussion**

The concept behind the introduction of Stokes parameters of the radar polarimetry has been described in the previous sections. The Stokes parameters have been concluded as efficient parameters to derive the polarimetric information of the radar. It is a beneficial approach for characterizing the scattering mechanism and properties of the surface through which the type of scattering i.e., surface scattering, double-bounce scattering, or volumetric scattering can be easily differentiated. The results obtained by applying the  $m$ - $\delta$ ,  $m$ - $\chi$ , and  $H$ - $\alpha$  decomposition techniques assist in retrieving the surface information of the craters. The scattering mechanism resulted from  $m$ - $\delta$  decomposition was different from other decomposition techniques. However, the results obtained from  $m$ - $\chi$  decomposition were similar to the scattering mechanism obtained by the Eigenvalue based  $H$ - $\alpha$  technique. Comparing the decomposition results with the results of CPR provided an advantage to understand more about the surface of the crater and for detecting the regions which have the possibility of the existence of water ice.

Impact craters have an intricate structure, formed by the impact of asteroids or meteorites with a transfer of energy. Being a complex process with no ground-truth, predictions cannot be procured, as it may imply imprecise detection and estimations in any planetary-related analysis work. Thus, the delineation of boundaries of such craters in itself is a challenge that is yet to be achieved[13]. The histogram-based extraction of the crater boundaries could not delineate the precise boundaries of the craters as compared to the ArcGIS tool which provided better results. It is observed that, in case the craters are to be extracted through visual interpretation or manual digitization, craters ejecta blanket suppresses the boundaries of the craters making it difficult to extract the craters.

#### **5. Conclusions**

The polarimetric decomposition techniques  $m$ - $\delta$ ,  $m$ - $\chi$ , and  $H$ - $\alpha$  have given profound results to characterize the surface through scattering mechanisms. All three techniques relatively contributed in describing the scattering mechanism of the surface of the craters. The Eigenvector decomposition technique characterizes the surface in terms of the degree of polarization and the scattering mechanisms. Since the validation of the researches in planetary studies is a big challenge, thus previous literature and researches have been considered as the main aspect to prove the findings. NASA has estimated that the rough and fresh surface of lunar craters which could be found transparent to radio signals lead to enhancements in the same reflections and thus concluding to high CPR values[14]. The CPR has provided a major contribution to the results of the decomposition techniques in defining the intensity of the pixel values of the regions through comparison between each other. However, the detection of the areas relating to the content of water-ice deposits is itself a huge finding to understand a planet. Since CPR alone cannot prove this theory; additional

parameters need to be included to verify the results. The analysis of the dielectric properties of the craters could bring an insight to verify the regions associating with the presence of water-ice deposits.

It has been concluded that the ArcGIS Crater tool is useful for delineating the boundaries of circular craters. However, if the crater is either irregular or elliptical the delineation of precise boundaries is relatively difficult. In the case of the histogram-based extraction approach to delineate the crater boundaries, the method uses the manipulation of histogram values to differentiate between the craters and the background, and thus crater with any shaped can be detected as well as delineated.

## References

- [1] "Is There an Atmosphere on the Moon?," 2013. [Online]. Available: [https://www.nasa.gov/mission\\_pages/LADEE/news/lunar-atmosphere.html](https://www.nasa.gov/mission_pages/LADEE/news/lunar-atmosphere.html).
- [2] "Lunar Atmospheric Composition." [Online]. Available: [https://www.lpi.usra.edu/lunar/missions/apollo/apollo\\_17/experiments/lace/](https://www.lpi.usra.edu/lunar/missions/apollo/apollo_17/experiments/lace/).
- [3] S. Mohan, A. Das, and M. Chakraborty, "Studies of polarimetric properties of lunar surface using Mini-SAR data," *Curr. Sci.*, vol. 101, no. 2, pp. 159–164, 2011.
- [4] S. Yue, L. He, Y. Wen, G. Lu, and H. Lin, "Shape characteristics-based extraction of lunar impact craters: using DEM from the Chang'E-1 satellite as a data source," *Ann. GIS*, vol. 19, no. 1, pp. 53–62, 2013, doi: 10.1080/19475683.2012.758656.
- [5] S. Saran, A. Das, S. Mohan, and M. Chakraborty, "Study of scattering characteristics of lunar equatorial region using Chandrayaan-1 Mini-SAR polarimetric data," *Planet. Space Sci.*, vol. 71, no. 1, pp. 18–30, 2012, doi: 10.1016/j.pss.2012.06.014.
- [6] P. V Jayasri, H. S. V. U. Sundari, E. V. S. Sita, and A. V. V Prasad, "M-delta Decomposition of Hybrid Dual- Polarimetric RISAT-1 SAR Data," *9th Int. Radar Symp.*, vol. IRSI-13, no. December, pp. 1–4, 2013.
- [7] R. K. Raney *et al.*, "The lunar mini-RF radars: Hybrid polarimetric architecture and initial results," *Proc. IEEE*, vol. 99, no. 5, pp. 808–823, 2011, doi: 10.1109/JPROC.2010.2084970.
- [8] K. Dasari and A. Lokam, "Exploring the Capability of Compact Polarimetry (Hybrid Pol) C Band RISAT-1 Data for Land Cover Classification," *IEEE Access*, vol. 6, pp. 57981–57993, 2018, doi: 10.1109/ACCESS.2018.2873348.
- [9] K. B. Bhavya, "Polarimetric modeling of Lunar surface for scattering information retrieval using mini-SAR data of Chandrayaan-1," 2013.
- [10] S. R. Cloude, D. G. Goodenough, and H. Chen, "Compact Decomposition Theory," *IEEE Geosci. Remote Sens. Lett.*, vol. 9, no. 1, pp. 28–32, Jan. 2012, doi: 10.1109/LGRS.2011.2158983.
- [11] A. S. Kiran Kumar and A. R. Chowdhury, "Terrain mapping camera for Chandrayaan-1," *J. Earth Syst. Sci.*, vol. 114, no. 6, pp. 717–720, 2005, doi: 10.1007/BF02715955.
- [12] T. Rajput, "Satellite-derived digital topography-based crater boundary detection and attribute measurements by segmentation and moments measure techniques," *Earth*, 2011.
- [13] T. Rajput, "SATELLITE-DERIVED DIGITAL TOPOGRAPHY-BASED CRATER BOUNDARY DETECTION AND ATTRIBUTE MEASUREMENTS BY SEGMENTATION AND MOMENTS MEASURE TECHNIQUES," 2011.

[14] “Mini-RF.” [Online]. Available:

[https://www.nasa.gov/mission\\_pages/Mini-RF/multimedia/feature\\_ice\\_like\\_deposits.html](https://www.nasa.gov/mission_pages/Mini-RF/multimedia/feature_ice_like_deposits.html).



© 2020 by the authors. Submitted for possible open access publication under the terms and conditions of the Creative Commons Attribution (CC BY) license (<http://creativecommons.org/licenses/by/4.0/>).